JGR Atmospheres

RESEARCH ARTICLE
10.1029/2023JD039447

The Influence of Southeastern South American Rainfall on Weather Patterns Over the Tropical Atlantic, Northwestern Africa and Western Europe

Siyu Zhao[1], Rong Fu[1], Hui Wang[2], and Fei-Fei Jin[3]

[1]Department of Atmospheric and Oceanic Sciences, University of California, Los Angeles, Los Angeles, CA, USA, [2]NOAA/NWS/NCEP/Climate Prediction Center, College Park, MD, USA, [3]Department of Atmospheric Sciences, School of Ocean and Earth Science and Technology, University of Hawai'i at Mānoa, Honolulu, HI, USA

Key Points:

- Southeastern South American rainfall can induce cross-equatorial propagation of Rossby wave (CEPRW) during boreal winter
- Such CEPRW increases high pressure and surface temperature anomalies over northwestern Africa and western Europe

Correspondence to:

S. Zhao,
siyu_zhao@atmos.ucla.edu

Citation:

Zhao, S., Fu, R., Wang, H., & Jin, F.-F. (2023). The influence of southeastern South American rainfall on weather patterns over the tropical Atlantic, northwestern Africa and western Europe. *Journal of Geophysical Research: Atmospheres*, *128*, e2023JD039447. https://doi.org/10.1029/2023JD039447

Received 13 JUN 2023
Accepted 4 OCT 2023

Abstract During boreal winter (December–February), the South American monsoon system (SAMS) reaches its annual maximum when upper-tropospheric westerly winds prevail over the equatorial Atlantic. Atmospheric dynamic model simulations suggest that Rossby waves generated over South America can propagate to and potentially influence weather patterns in the Northern Hemisphere (NH). However, observational evidence has been absent previously. Here we focus on southeastern South American (SESA) precipitation anomalies, which can characterize intraseasonal rainfall variability of the SAMS. Since tropical "westerly duct" and convective heating are important factors for cross-equatorial propagation of Rossby wave (CEPRW), we identify two groups of events based on the two factors. By comparing the events associated with both SESA rainfall and tropical westerlies to the events associated with tropical westerlies only, we find that an anomalous Rossby wave train is triggered by precipitation anomalies over SESA, propagates in the southwest–northeast direction, and subsequently crosses the equator. Over a period of 4 days, near-surface temperature over northwestern Africa and western Europe becomes warmer, accompanied by increased surface downward longwave radiation and precipitable water. The equatorward propagating Eliassen–Palm flux anomalies originated from SESA support the evidence of CEPRW. Simulations using a time-dependent linear barotropic model forced by prescribed divergence anomalies over SESA further confirm that SESA rainfall can influence the NH weather patterns through CEPRW. Knowledge of this study will help us better understand and model interhemispheric teleconnections over the American–Atlantic–African/European sector.

Plain Language Summary The South American monsoon system dominates the seasonal cycle of precipitation over South America and reaches maximum during boreal winter (December–February). Whether and how the South American monsoon related rainfall influences weather patterns in the Northern Hemisphere (NH) has been previously unclear. Using observational analyses, we find that rainfall variability over southeastern South America (SESA) can trigger atmospheric waves, which travel northeastward and cross the equator. As these waves propagate and transport momentum downstream, they increase precipitable water, surface downward longwave radiation, and thus surface temperature over northwestern Africa and western Europe in about 4 days. Numerical model simulations confirm that atmospheric waves generated by SESA rainfall can produce observed weather patterns in the NH. Knowledge of this study can advance our understanding of connections of weather patterns between hemispheres over the American–Atlantic–African/European sector.

1. Introduction

The South American monsoon system (SAMS), the world's second largest convective center, reaches its annual maximum in boreal winter (December–February, DJF) (e.g., Jones & Carvalho, 2002; Liebmann & Mechoso, 2011; Vera et al., 2006; Zhou & Lau, 1998). Increase of evapotranspiration (ET) over the rainforest in boreal fall initiates large-scale convections and rainy season over Amazonia (e.g., Li & Fu, 2004; Wright et al., 2017). Latent heating released by Amazonian convection (e.g., Lenters & Cook, 1997; Silva Dias et al., 1983) drives monsoonal northeasterly flow, which is from the Atlantic and subsequently deflected southward by the Andes (Boers et al., 2013; Bookhagen & Strecker, 2008; Liebmann et al., 2004; Marengo et al., 2004). The moist air flow sustained by high ET over the rainforest (Wright et al., 2017) leads to strong rainfall anomalies over southeastern Brazil and La Plata (e.g., Berbery & Barros, 2002; Dominguez et al., 2022; Zhou & Lau, 1998), exerting

strong impacts on human activities such as cultivation and hydroelectricity production over that region (Carvalho et al., 2002; Marengo et al., 2013; Zhang et al., 2023).

During boreal winter, a dipolar rainfall pattern with two centers over the South Atlantic Convergence Zone and southeastern South America (SESA; similar to the region of La Plata Basin) has been identified using an empirical orthogonal function (EOF) analysis (e.g., Cherchi et al., 2014; Nogués-Paegle & Mo, 1997; Vera et al., 2018). This dipolar structure is known as the South American rainfall dipole and characterizes the intraseasonal rainfall variability of the SAMS (Boers et al., 2014; Díaz et al., 2020; Marengo et al., 2012; Paegle et al., 2000; Zamboni et al., 2010). SESA rainfall anomalies form the southern component of the dipolar pattern and relate to anomalies in large-scale climatic features such as El Niño–Southern Oscillation, Pacific–South American (PSA), Antarctic Oscillation, and Madden–Julian Oscillation (e.g., Grimm et al., 2000; Mo & Paegle, 2001; Silvestri & Vera, 2003; Vera et al., 2018). Specifically, Gelbrecht et al. (2018) found that rainfall anomalies over SESA are coherent with the Southern Hemisphere (SH) Rossby waves, which may be related to the PSA modes (Ghil & Mo, 1991; Mo & Ghil, 1987; Mo & Paegle, 2001). As the SAMS peaks in boreal winter, atmospheric circulations over the North Atlantic–western Europe sector exhibit substantial synoptic-to-intraseasonal variabilities (e.g., Ayarzagüena et al., 2018; Feldstein, 2003; Gulev et al., 2002; Luo et al., 2011). To our knowledge, the influence of precipitation anomalies of the SAMS, especially those related to SESA rainfall, on the Northern Hemisphere (NH) weather patterns through cross-equatorial propagation of Rossby wave (CEPRW) has not been documented in the literature.

Previous studies have widely documented interhemispheric teleconnections, which are involved with mechanisms such as CEPRW (e.g., Tomas & Webster, 1994; Webster & Holton, 1982; Zhao et al., 2015), extratropical forced equatorial Kelvin waves (e.g., Hoskins & Yang, 2000; Liebmann et al., 2009; Mayta et al., 2021; Zhao & Fu, 2022), low-level cross-equatorial flow linked to monsoonal circulations (e.g., Lau & Li, 1984; Wang & Fu, 2002; Zhong et al., 2023), and shallow meridional circulations (e.g., Bowerman et al., 2017; Zhang et al., 2008). Among these mechanisms, CEPRW has been investigated in the literature through theoretical wave studies, observational analyses, and numerical experiments, mostly over the Pacific sector (Chen et al., 2022; Hsu & Lin, 1992; Karoly, 1983; Li et al., 2015, 2019; Tomas & Webster, 1994; Webster & Holton, 1982; Zhao et al., 2015, 2019). Two factors are important for CEPRW. The first one is the upper-tropospheric westerly wind over tropical regions, referred to as the "westerly duct," enabling Rossby waves to propagate from one hemisphere to the other (Charney, 1969; Dickinson, 1968; Hsu & Lin, 1992; Tomas & Webster, 1994; Webster & Holton, 1982). The diabatic heating related to convections over the source region is also important because it can trigger atmospheric trough/ridge patterns that form Rossby wave train propagating downstream (Danard, 1964; Emanuel et al., 1987; Golding, 1984; Gong et al., 2020; Gutowski et al., 1992; Gyakum, 1983; Lapeyre & Held, 2004; Wirth et al., 2018; Zhao et al., 2018). Previous studies have shown that convective heating in one hemisphere can influence weather and climate in the other and such influence may be involved with CEPRW (e.g., Ambrizzi & Hoskins, 1997; Chen et al., 2022; Yang & Webster, 1990; Zhao et al., 2019). For example, tropical heating over the tropical Indian and Pacific Oceans and Maritime Continent can influence the SH climate through the southward propagation of Rossby waves (Chen et al., 2022; Zhao et al., 2019).

For the Atlantic sector, Li et al. (2019) extended previous work and explored windows and barriers for CEPRW using a wave ray tracing method. They found that over the South American–Atlantic sector the main CEPRW from SH to NH during boreal winter follows a great circle with a tilt in the southwest–northeast direction. Evidence for the South American influence on the North Atlantic is suggested by numerical model simulations. For example, a Rossby wave train propagating from South America across North Atlantic towards northern Europe is a response to an idealized diabatic heating anomaly near northwestern South America (0°, 90°W) in a barotropic model simulation (Ambrizzi & Hoskins, 1997). Other studies found that Amazon deforestations can result in anomalous Rossby wave trains that modify atmospheric circulations in remote areas (e.g., Gedney & Valdes, 2000; Snyder, 2010; Werth & Avissar, 2002). Specifically, Snyder (2010) showed that northeastward propagating Rossby waves from South America are excited by a weakening of deep tropical convection due to Amazon deforestations and such Rossby waves can influence northeastern Atlantic and Europe by changing storm tracks.

This study aims to understand the influence of SESA rainfall on the NH circulation and weather patterns using both observational analyses and dynamic model simulations. We will first identify relevant events with anomalous rainfall over SESA. We will measure the Eliassen–Palm flux (EP-flux) associated with the selected rainfall

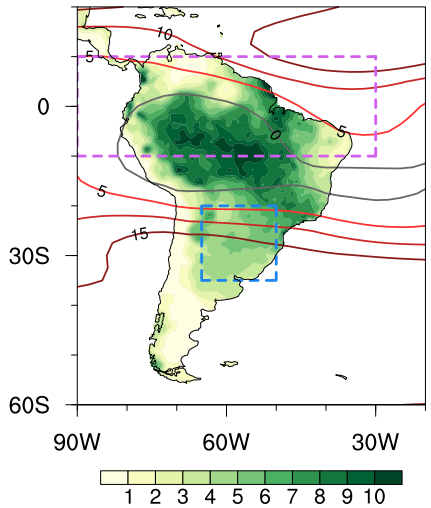

Figure 1. Climatological rainfall (mm day^{-1}; shading) and 300 hPa zonal wind (m s^{-1}; contours) during boreal winter from 1979 to 2019. For contours, red and gray lines represent positive values and zero, respectively. The region of the U300 index is shown within the purple box (10°S–10°N, 30°W–90°W). The region of southeastern South American rainfall index is shown within the blue box (20°S–35°S, 50°W–65°W).

events to examine the role of CEPRW in the interhemispheric teleconnection. EP-flux is a widely used diagnostic tool for wave propagation and is suitable for analyzing meridionally propagating waves (e.g., Dwyer & O'Gorman, 2017; Edmon et al., 1980; Hu et al., 2018; Lieberman, 1999). Finally, we will use a time-dependent barotropic model (Ting, 1996) to simulate the effect of SESA rainfall by prescribing a divergence anomaly (heating) over SESA. The examination of the atmospheric response to a prescribed diabatic heating anomaly is a commonly used method (e.g., Li, 2006; Li et al., 2015; Lutsko, 2018; Zhao et al., 2019; Zhu & Li, 2016). The remainder of the paper is organized as follows. Data and methodology are described in Section 2. Section 3.1 identifies anomalous rainfall events over SESA. Section 3.2 examines CEPRW associated with selected rainfall events. Barotropic model simulations will be shown in Section 3.3. A summary and additional discussion are provided in Section 4.

2. Data and Methodology

2.1. Data

Daily data during DJF from 1979 to 2019 are used in this study. The precipitation is from National Oceanic and Atmospheric Administration (NOAA) Climate Prediction Center (CPC) Global Unified Gauge-Based Analysis of Daily Precipitation with a spatial resolution of 0.5° (Chen et al., 2008). The near-surface (10 m) zonal and meridional winds and multilevel geopotential height, zonal and meridional winds, and air temperature are from the European Center for Medium-Range Weather Forecasts fifth-generation reanalysis (ERA5) at the spatial resolution of 2.5° (Copernicus Climate Change Service, 2017). The near-surface air temperature (2 m), surface downward longwave radiation (LW), and precipitable water (also known as precipitable water vapor or total column water vapor) are also from ERA5 at the resolution of 1.0°.

2.2. Indices Related to SESA Rainfall and "Westerly Duct"

Tropical zonal wind at 300 hPa averaged over 10°S–10°N, 30°W–90°W (the purple box in Figure 1) is referred to as the U300 index, while precipitation anomalies averaged over 20ºS–35ºS, 50ºW–65ºW (the blue box in Figure 1) is referred to as the SESA rainfall index. The region of precipitation anomalies follows that of the southern component of the South American rainfall dipole via the EOF analysis (Cherchi et al., 2014; Nogués-Paegle & Mo, 1997; Vera et al., 2018). Two groups of selected events in boreal winter during 1979–2019 are identified in this study. Group 1 is associated with SESA rainfall with a requirement of daily SESA rainfall index greater than one standard deviation of the daily precipitation for the calendar day (1σ). Additionally, we require that daily U300 index is greater than 5 m s^{-1} to allow latitudinal propagation across the equator. The tropical westerly wind generally extends from 500 to 100 hPa and has both intraseasonal and synoptic timescales (with periods spanning from 2.5 to 40 days and from 50 to 55 days) (not shown). When consecutive days satisfy these requirements, only the first day is used as Day 0 for the composite (e.g., Bowerman et al., 2017). The results are not sensitive to the rainfall threshold ranging from 0.5σ to 2σ and U300 threshold ranging from 1 m s^{-1} to 8 m s^{-1}. We identify a total of 168 events for Group 1 and the maximum duration of these events is 5 days. Group 2 is associated only with tropical westerlies (U300 index greater than 5 m s^{-1}) and a total of 1,374 days meet this criterion.

2.3. Eliassen–Palm Flux

EP-flux is a vector quantity in the latitude–pressure plane and the direction and magnitude of the flux indicate the relative importance of eddy heat flux and momentum flux. Following Equations 3.1a and 3.1b of Edmon et al. (1980), we calculate the EP-flux in horizontal ($F_{(\phi)}$) and vertical ($F_{(p)}$) directions in a spherical coordinate at vertical pressure levels:

$$F_{(\phi)} = -r\cos\phi\,\overline{u'v'},$$

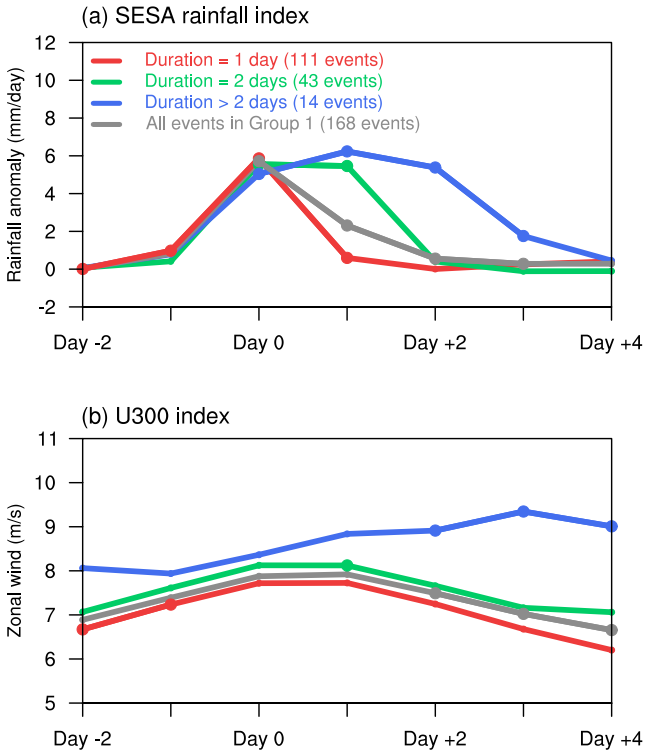

Figure 2. (a) The evolution of daily southeastern South American rainfall index (mm day^{-1}) for all selected events in Group 1 and the events with the duration of 1 day, 2 days, and more than 2 days, respectively, from Day −2 to Day +4. (b) Same as (a), but for daily U300 index (m s^{-1}). The days with large dots indicate that the index for the selected events in Group 1 is significantly (at the 95% level) different from that for Group 2 according to the bootstrap test.

$$F_{(p)} = f r \cos\phi \, \overline{v'\theta'} / \overline{\theta}_p, \tag{1}$$

where ϕ, r, and f are latitude, Earth radius, and Coriolis parameter, respectively. u, v, and θ are zonal and meridional winds and potential temperature, respectively. Over-bars and primes denote zonal means and departures therefrom, respectively. Subscripts without a parenthesis denote partial differentiation. The divergence of the EP-flux is calculated following Equation 3.2 of Edmon et al. (1980):

$$\mathrm{Div}(\boldsymbol{F}) = \frac{1}{r\cos\phi}\frac{\partial}{\partial\phi}(F_{(\phi)}\cos\phi) + \frac{\partial}{\partial p}(F_{(p)}). \tag{2}$$

2.4. Barotropic Model

We use a time-dependent barotropic model based on the barotropic vorticity equation linearized about a mean state (Ting, 1996). The forcing in the model is prescribed divergence over a selected rainfall domain and the divergence anomaly could be shown as

$$D(\lambda,\phi) = A\, e^{-\left(\frac{\lambda-\lambda_0}{b}\right)^2} e^{-\left(\frac{\phi-\phi_0}{b}\right)^2}, \tag{3}$$

where λ and ϕ are longitude and latitude, respectively, for a point. The forcing center is at longitude λ_0 and latitude ϕ_0. A is amplitude, which is 1.2×10^{-6}. b is e-folding scale (equal to 5° for zonal and meridional directions), so that the divergence anomaly is close to zero outside the selected rainfall domain.

In addition, all the mean and anomaly fields are expanded with spherical harmonics (spectral model) and truncated to rhomboidal wavenumber 15. The horizonal resolution is 7.5° and 4.5° for longitude and latitude, respectively. One timestep is 10 min. The biharmonic diffusion coefficient and Rayleigh friction time scale are 2×10^{16} m^2 s^{-1} and 8 days, respectively. A detailed description of the barotropic model can be found in Ting (1996).

3. Results

3.1. Southeastern South American Rainfall Variability

Figure 1 shows long-term climatology (averaged from 1979 to 2019) of the South American rainfall and 300-hPa zonal wind during boreal winter (DJF). Due to the presence of the SAMS (e.g., Jones & Carvalho, 2002; Liebmann & Mechoso, 2011; Vera et al., 2006; Zhou & Lau, 1998), the heaviest rainfall occurs over the Amazon basin and its magnitude gradually drops from the tropics to subtropics. The rainfall within the blue box represents the southern component of the South American rainfall dipole identified in previous studies (Cherchi et al., 2014; Nogués-Paegle & Mo, 1997; Vera et al., 2018). In the upper troposphere, westerly wind zones appear over the equatorial Atlantic, allowing Rossby waves propagating from the SH to NH (e.g., Hsu & Lin, 1992; Tomas & Webster, 1994; Webster & Holton, 1982). Despite westerlies over the equatorial Atlantic, a strong easterly barrier appears over the Amazon basin due to the presence of an upper-tropospheric high pressure center over southern Amazon in boreal winter, making it hard for Rossby waves to propagate across the equator there (Li et al., 2019).

Following the method in Section 2.2, two groups of the events in DJF during 1979–2019 are identified. Events in Group 1 are influenced by SESA rainfall and tropical westerlies, and those in Group 2 are influenced by tropical westerlies only. Figure 2a shows the evolution of daily SESA rainfall index for all selected events in Group 1 and the events of Group 1 with the duration of 1 day, 2 days, and more than 2 days, respectively. For all selected events in Group 1 (gray line), Day 0 represents the peak day of the rainfall. The rainfall index from Day −1 to Day +3 is significantly different from that in Group 2 at the 95% level according to a bootstrap significance test (Efron & Tibshirani, 1994), indicating that choosing 1σ as a threshold for strong precipitation anomalies can truly separate the two groups. We calculate the duration (i.e., the total number of consecutive days with daily precipitation

anomalies greater than 1σ for an event) of the selected events in Group 1. The result shows that two-thirds of the events are short-lasting rainfall events, while around 8% of the events last 3 days or more. By definition, the rainfall index for the events with 1-day, 2-day, and more than 2-day duration peaks on Day 0 (red line), on both Day 0 and Day +1 (green line), and from Day 0 to Day +2 (blue line), respectively.

Figure 2b shows the corresponding evolution of daily U300 index for Group 1. The value of the zonal wind at 300 hPa gradually increases when the duration of the events increases. To evaluate whether SESA rainfall anomalies are influenced by upper-tropospheric zonal winds over the tropics, we break down SESA rainfall by events where the tropical westerlies are active (i.e., U300 > 5 m s^{-1}; as in Group 1) and events where they are not (i.e., U300 $\leq$ 5 m s^{-1}). The result shows that the events with inactive tropical westerlies exhibit a very similar plot compared to the gray line in Figure 2a, indicating that SESA rainfall is not influenced by upper-tropospheric zonal wind over the tropics.

3.2. Cross-Equatorial Waves Associated With SESA Rainfall

In this section, we examine atmospheric circulations and weather patterns associated with SESA rainfall. Since the lower-level wave train dissipates due to surface friction (e.g., Hsu & Lin, 1992; Wallace & Gutzler, 1981), we focus on the upper-level wave train patterns and examine how they influence the NH circulations. Standardization of circulation patterns are used for a better representation in the tropics (e.g., Bowerman et al., 2017). Figure 3 shows the evolution map of atmospheric circulations associated with Group 2. Symmetric circulation

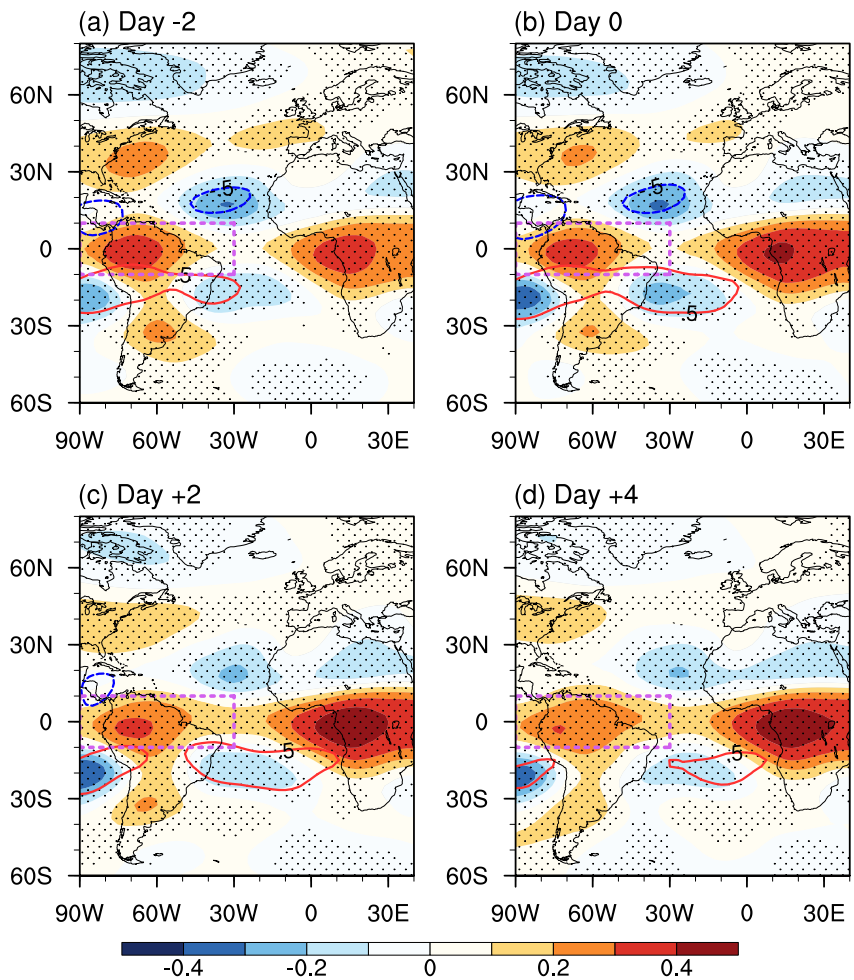

Figure 3. (a–d) Composite anomalies of standardized 200 hPa geopotential height (shading) and standardized 200 hPa streamfunction (contours) for the events in Group 2 from Day −2 to Day +4. For contours, solid red and dashed blue lines represent positive and negative values, respectively. Stippling indicates areas significant at the 95% level according to the bootstrap test. The region of the U300 index is shown within the purple box (10°S–10°N, 30°W–90°W).

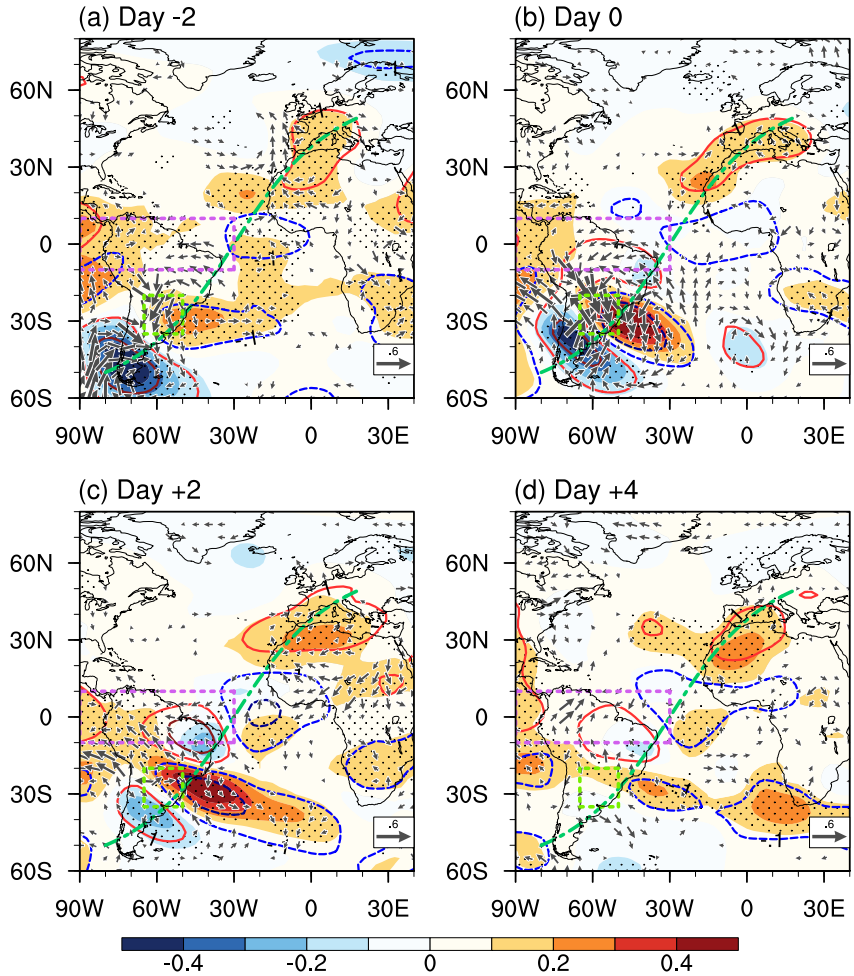

Figure 4. (a–d) Composite of standardized 200 hPa geopotential height (shading), standardized 200 hPa streamfunction (contours), and standardized near-surface (10 m) wind (vectors) anomalies for the difference between Group 1 and Group 2 from Day −2 to Day +4. For contours, solid red and dashed blue lines represent positive and negative values, respectively. Stippling indicates areas significant at the 95% level according to the bootstrap test. Vectors significant at the 95% level are shown. The region of the U300 index is shown within the purple box (10°S–10°N, 30°W–90°W). The region of southeastern South American rainfall index is shown within the green box (20°S–35°S, 50°W–65°W). The green curve indicates the pathway of the wave train.

pattern about the equator can be seen from two days before the peak of U300 (Figure 3a) to four days after its peak (Figure 3d). The magnitude of circulation centers over the NH becomes weaker after Day 0 (Figures 3b–3d). There is no clear evidence of northward propagated cross-equatorial waves in the composite of Group 2, which is possibly dominated by quasi-stationary Rossby waves.

Figure 4 shows composite maps for the difference between Group 1 and Group 2 from Day −2 to Day +4. Such maps indicate the net effect of SESA rainfall on circulation patterns. Geopotential height anomalies have the same sign as streamfunction anomalies in the NH, but the opposite sign in the SH. Before the peak of SESA rainfall (Day −2), a high pressure center exists over western Europe and northwestern Africa, but it may not be related to CEPRW because wave signals over the tropics are quite weak (Figure 4a). During the peak of SESA rainfall (Day 0), a Rossby wave train propagates downstream in a southwest–northeast direction over the South American–Atlantic sector, and ridge/trough centers with large magnitude mainly appear over the subtropics (Figure 4b). From Day 0 to Day +2, negative geopotential height anomalies (also the dipole of streamfunction anomalies) near the equator intensify, accompanied by intensified high pressure anomalies over western Europe and northwestern Africa (Figures 4b and 4c). On Day +4, the wave train weakens, leading to a shrinking of the high pressure center over western Europe and northwestern Africa (Figure 4d). These results provide

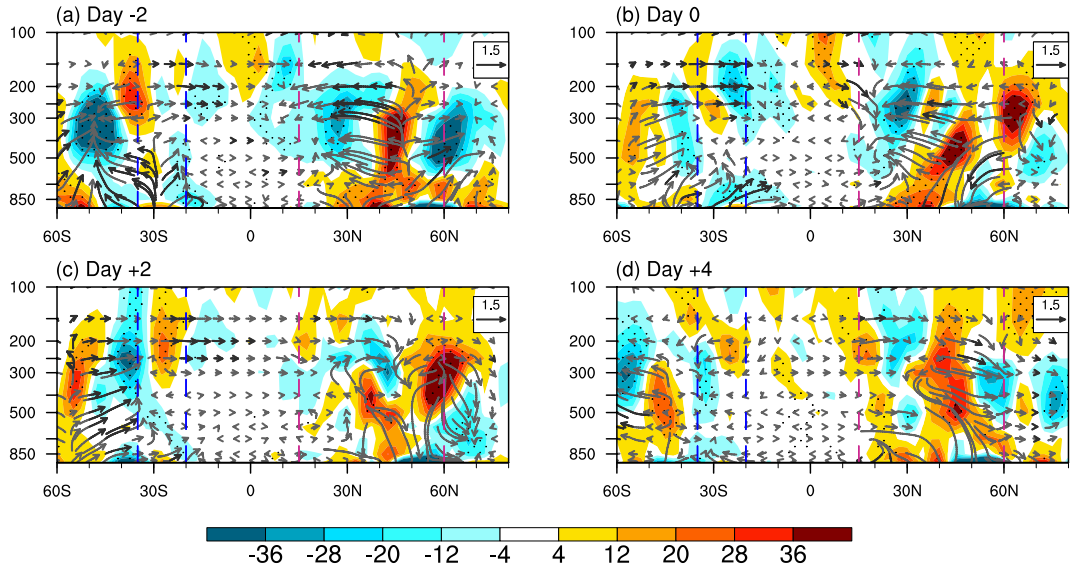

Figure 5. (a–d) Same as Figure 4, but for composite of Eliassen-Palm flux (vectors with units of 10^5 Pa m^2 s^{-2} for vertical vectors and 2×10^7 m^3 s^{-2} for horizontal vectors) and associated divergence (m^2 s^{-2}; shading) anomalies. Vectors significant at the 95% level are shown in black. The region between the two dashed blue lines represents southeastern South America, and that between the two dashed red lines denote western Europe and northwestern Africa.

evidence that CEPRW associated with SESA rainfall can intensify high pressure anomalies over the NH. The pathway of the CEPRW follows a great circle with a tilt in the southwest–northeast direction, as suggested by Li et al. (2019).

In addition, from Day −2 to Day 0, the South American low-level jet (Montini et al., 2019) brings abundant moisture to SESA, causing mesoscale convective systems and strong precipitation anomalies (Figures 4a and 4b; Boers et al., 2013, 2014; Durkee et al., 2009; Salio et al., 2007). Strong precipitation anomalies can generate Rossby wave train by anomalous latent heating associated with cloud and rainfall formation through baroclinic processes (e.g., Danard, 1964; Emanuel et al., 1987; Golding, 1984; Gong et al., 2020; Gutowski et al., 1992; Gyakum, 1983; Lapeyre & Held, 2004; Wirth et al., 2018; Zhao et al., 2018). The wave train pattern near SESA exhibits a baroclinic structure in the vertical, with upper-level geopotential height anomalies appearing to the southwest of the lower-level geopotential height anomalies (not shown). The low-level flow weakens significantly after the peak of SESA rainfall (Figures 4c and 4d).

To further investigate the role of SESA rainfall and associated CEPRW, we show EP-flux anomalies for the difference between the two groups on a latitude–pressure plane (Figure 5). From two days before the peak of SESA rainfall, upward EP-flux anomalies propagate vertically from the lower troposphere near 30ºS, indicating that meridional heat flux dominates (Figures 5a and 5b). Equatorward propagating EP-flux anomalies, mainly confined in the upper troposphere, start to cross the equator from Day +2 and end around Day +4 (Figures 5c and 5d), accompanied by a series of divergence/convergence anomalies that can accelerate/decelerate westerly winds (Chen et al., 2002; Chen & Wu, 2018). The equatorward EP-flux anomalies suggest that meridional flux of zonal momentum dominates. Downward EP-flux anomalies appear over 15ºN–60ºN on Day +2 (Figure 5c) and likely influence the lower tropospheric circulation and surface weather over western Europe and northwestern Africa. The EP-flux propagation in Figure 5 is consistent with the CEPRW in Figure 4, further confirming that SESA rainfall generates upper-level Rossby wave trains that cross the equator and influence the NH circulations.

Figure 6 shows the change in near-surface temperature and lower-tropospheric circulations over the Eurasian–African sector before and after the peak of SESA rainfall. Before CEPRW reaches the extratropical NH, positive temperature anomalies over western Europe are associated with a high pressure center, whose magnitude reduces from Day −2 to Day 0 (Figures 6a and 6b). After Day 0, the high pressure center significantly expands and intensifies over northern Africa, much stronger than that on Day −2, indicating the effect of CEPRW (Figure 6c). The high pressure center is accompanied by near-surface anticyclonic wind anomalies. As the circulation patterns

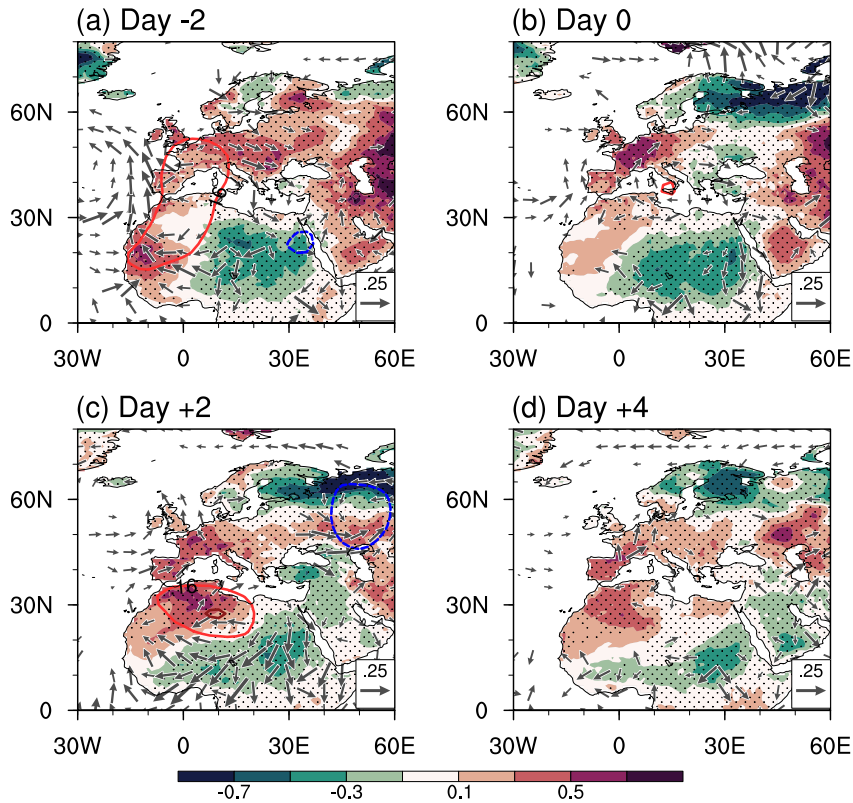

Figure 6. (a–d) Same as Figure 4, but for composite of near-surface temperature (ºC; shading), standardized 700 hPa streamfunction centers (contours), and standardized near-surface wind (vectors).

change, near-surface temperature anomalies also change. Over Europe, positive temperature anomalies over western Europe increase from Day 0; negative temperature anomalies over eastern Europe decrease in magnitude; and negative temperature anomalies over northern Europe generally stay the same (Figures 6b and 6c). The largest change in temperature anomalies occur over northwestern Africa on Day +2, with the value greater than 0.5ºC. Such an increase of positive temperature anomalies corresponds to an intensification of upper-level high pressure anomalies shown in Figure 4, as well as downward EP-flux anomalies around 15ºN–60ºN in Figure 5. On Day +4, temperature anomalies over western Europe and northwestern Africa decrease due to weakened CEPRW (Figure 6d).

We also evaluate surface radiation change associated with near-surface temperature change. We find that change in surface downward LW (shading; Figure 7) is consistent with change in near-surface temperature (Figure 6), while the change in surface downward shortwave radiation is not (not shown). Over western Europe and northwestern Africa, LW gradually increases from Day 0 and weakens on Day +4. Such positive LW anomalies are linked to positive precipitable water anomalies (contours) that provide moisture in the atmosphere and thus emit LW back to the surface. To further examine the relationship among LW, near-surface temperature, and precipitable water, we calculate the spatial correlation between near-surface temperature and LW and that between precipitable water and LW over western Europe and northwestern Africa (15ºN–60ºN, 20ºW–30ºE) for all the events in Group 1. Figure 8 shows the box plot for the spatial correlation coefficients, the mean/medium of which is significant at the 99% level. The result suggests that (a) the correlation between each pair of the variables generally stays the same (despite the large variation in the minimum value) during the evolution of the event (i.e., from Day −2 to Day +4) and (b) the relationship between LW and precipitable water is closer than that between LW and near-surface temperature. In addition, we examine the change in precipitation corresponding to CEPRW. The difference in precipitation between the two groups is insignificant over western Europe and northwestern Africa (not shown), despite positive precipitable water anomalies shown in Figure 7. Such insignificant precipitation anomalies are probably due to general dry conditions on surface, especially the Sahara Desert over northern Africa.

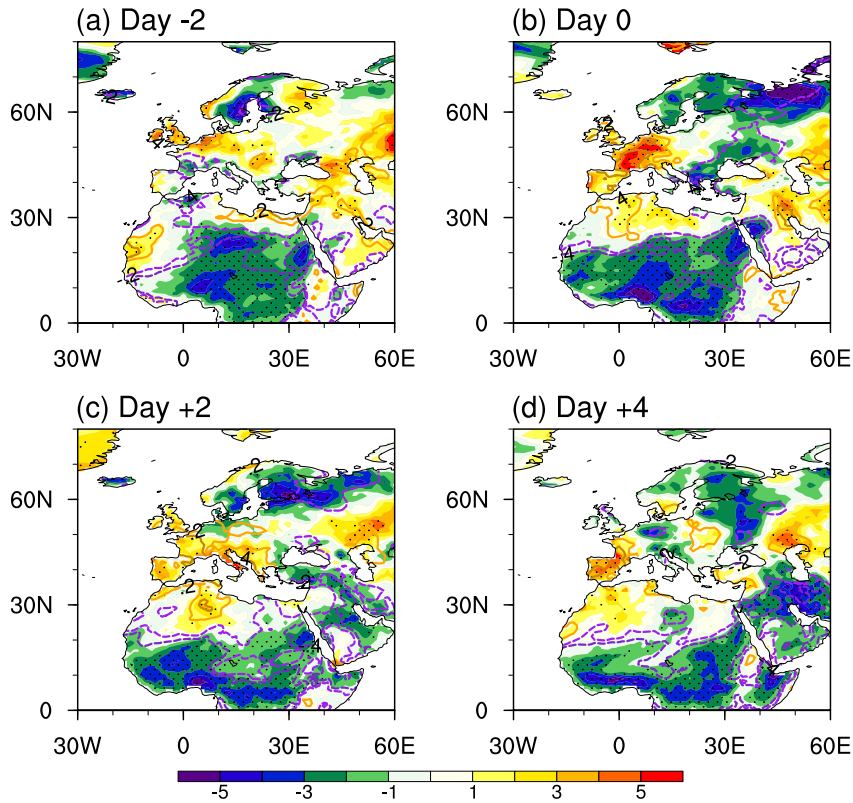

Figure 7. (a–d) Same as Figure 4, but for composite of longwave radiation (W m^{-2}; shading) and precipitable water (kg m^{-2}; contour). For contours, solid yellow and dashed purple lines represent positive values and negative values, respectively.

3.3. Barotropic Model Simulations

To simulate CEPRW triggered by SESA rainfall, we force a time-dependent linear barotropic model (Ting, 1996) by prescribing divergence anomalies over SESA. We use composite 200 hPa zonal and meridional winds of all selected events of Group 1 on Day 0 (peak day of the rainfall) as a basic state (background flow) for the linear barotropic model. We use 200 hPa wind fields as a basic state because the CEPRW mainly occurs in the upper troposphere between 100 and 300 hPa (Figure 5). The composite map of the zonal wind at 200 hPa (U200; Figure 9a) is similar to the climatological 200 hPa zonal wind during boreal winter. As shown in Figure 2a (gray line), the average duration of the events is around 4 days, that is, growing from Day −1, peaking on Day 0, decaying on Day +1, and ending on Day +2. Thus, we create time-varying forcing starting from Day −1. The prescribed divergence anomaly (Equation 3) for SESA rainfall on Day 0 (i.e., the peak of the rainfall) is shown in Figure 9b. The divergence anomaly field looks asymmetric because the center of the anomaly is not right at a grid point of the model. For other days, a coefficient is applied to Figure 9b in order to be consistent with evolution of observed SESA rainfall anomalies. For example, coefficients for Day −1, Day +1, and Day +2 are 0.23, 0.40, and 0.09, respectively.

Figure 10 shows that the divergence anomaly generates a Rossby wave train propagating from South America via the equator towards western Europe and northwestern Africa following a great circle (green line) from Day 0 to Day +4. The timing and general locations of simulated anomalous centers of streamfunction anomalies, that is, negative anomalies over SESA and tropical eastern Atlantic–western Africa sector and positive anomalies over equatorial South America and western Europe–northwestern Africa, broadly resemble the observations (Figure 10 vs. Figure 4). The shrinking of high pressure anomalies over western Europe and northwestern Africa is also well captured by the model on Day +4 (Figure 10f), corresponding to the observations on Day +4 (Figure 4d). Discrepancies in the exact pattern and location are mainly resulted from the simplicity of the model, for example, ignoring baroclinic processes that intrinsically affect initial perturbations triggered by local precipitation anomalies (e.g., Held et al., 1985). A better comparison of the CEPRW between model simulations and observations is expected if we switch to a more sophisticated model.

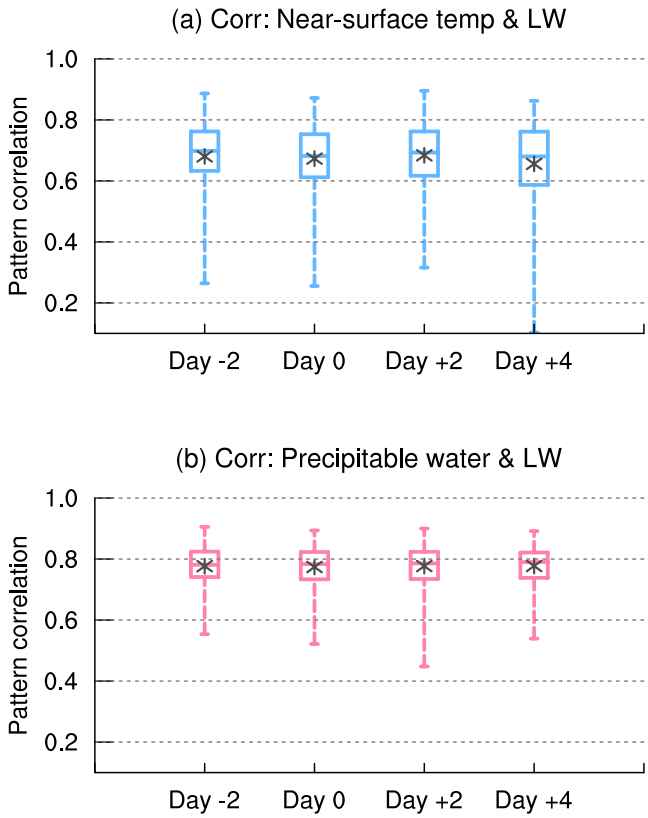

Figure 8. (a) Box plot for the minimum, 25th percentile, median, 75th percentile, and maximum of the spatial correlation between near-surface temperature and longwave radiation (LW) over western Europe and northwestern Africa for the events in Group 1 from Day −2 to Day +4. (b) Same as (a), but for the spatial correlation between precipitable water and LW. The asterisk denotes the mean of the correlation.

4. Summary and Discussion

This study investigates the influence of South American rainfall on the NH weather patterns during boreal winter and examines the role of CEPRW in the interhemispheric teleconnection. In particular, we focus on the southern component of the South American rainfall dipole, that is, SESA rainfall (e.g., Boers et al., 2014; Cherchi et al., 2014; Díaz et al., 2020; Marengo et al., 2012; Nogués-Paegle & Mo, 1997; Paegle et al., 2000; Vera et al., 2018). Two groups of the events in DJF during 1979–2019 are identified, with one group associated with both SESA rainfall and tropical westerlies and the other group associated with tropical westerlies only. The first group includes two factors that may induce CEPRW: diabatic heating related to convections and "westerly duct," while the second group only has "westerly duct." The difference in composite maps of selected events between the two groups represents the net effect of SESA rainfall on circulations and surface weather patterns.

Rainfall anomalies over SESA can trigger an upper-tropospheric anomalous Rossby wave train through anomalous latent heat release (e.g., Gong et al., 2020; Wirth et al., 2018; Zhao et al., 2018). Over a period of 4 days, the Rossby wave train crosses the equator following a great circle with a tilt in the southwest–northeast direction, and high pressure anomalies over western Europe and northwestern Africa are intensified due to the CEPRW, which is further confirmed by equatorward propagating EP-flux anomalies. The CEPRW can also influence the NH surface fields. Near-surface temperature anomalies over northwestern Africa increase significantly, accompanied by lower-tropospheric high pressure anomalies and anticyclonic wind anomalies. The temperature change over Europe is not as significant as that over northwestern Africa, but there is a temperature increase over Europe in general. The surface downward LW is also increased over western Europe and northwestern Africa, as a result of increased precipitable water. Such variations of LW can at least partly explain near-surface temperature anomalies associated with CEPRW. Finally, we apply a time-dependent linear barotropic model by prescribing a divergence anomaly over SESA. The timing and general locations of simulated anomalous centers of streamfunction anomalies broadly resemble the observations, further confirming the role of SESA rainfall and generated CEPRW in the NH weather.

This study provides observational evidence for a previously overlooked physical mechanism that influences weather patterns over northwestern Africa and western Europe. Knowledge of this study represents a first step to

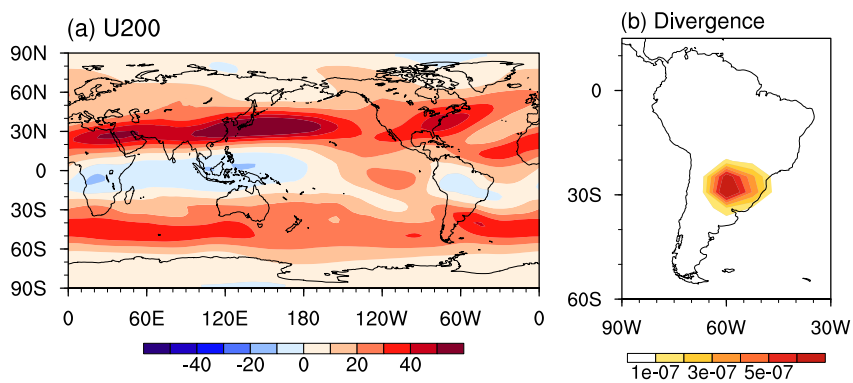

Figure 9. (a) The basic state represented as composite 200 hPa zonal wind (m s^{-1}) of all the selected events of Group 1 during the peak day of the rainfall. (b) The divergence anomaly (s^{-1}) for prescribed heating over southeastern South American on Day 0.

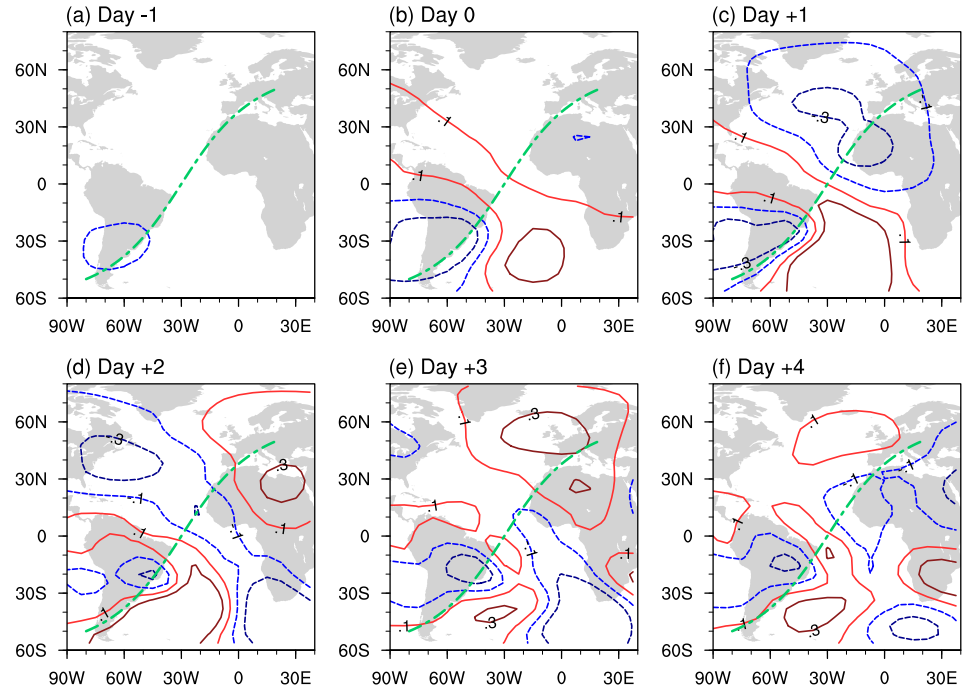

Figure 10. (a–f) The barotropic model simulation of the 200 hPa anomalous streamfunction (10^6 m^2 s^{-1}) responses 0–5 days after the forcing. Solid red and dashed blue lines represent positive and negative values, respectively. The green curve is the pathway of the observed wave train shown in Figure 4.

advance our understanding of interhemispheric teleconnections over the American–Atlantic–African/European sector, which has received little attention previously. The future work includes the consideration of baroclinic and nonlinear processes involved with CEPRW and investigation of the relationship between CEPRW and PSA modes.

Data Availability Statement

All the data used in this study are available online. The daily precipitation data is from NOAA CPC (NOAA CPC, 2008). The ERA5 reanalysis data is from Copernicus Climate Change Service (2017). The links to the data are provided in the reference.

Acknowledgments
We thank the three anonymous reviewers for their insightful comments. This study is supported by the National Science Foundation (Award Number 1917781).

References

Ambrizzi, T., & Hoskins, B. J. (1997). Stationary Rossby-wave propagation in a baroclinic atmosphere. *Quarterly Journal of the Royal Meteorological Society*, *123*(540), 919–928. https://doi.org/10.1002/qj.49712354007

Ayarzagüena, B., Ineson, S., Dunstone, N. J., Baldwin, M. P., & Scaife, A. A. (2018). Intraseasonal effects of El Niño–Southern Oscillation on North Atlantic climate. *Journal of Climate*, *31*(21), 8861–8873. https://doi.org/10.1175/JCLI-D-18-0097.1

Berbery, E. H., & Barros, V. R. (2002). The hydrologic cycle of the La Plata Basin in South America. *Journal of Hydrometeorology*, *3*(6), 630–645. https://doi.org/10.1175/1525-7541(2002)003<0630:THCOTL>2.0.CO;2

Boers, N., Bookhagen, B., Marwan, N., Kurths, J., & Marengo, J. (2013). Complex networks identify spatial patterns of extreme rainfall events of the South American monsoon system. *Geophysical Research Letters*, *40*(16), 4386–4392. https://doi.org/10.1002/grl.50681

Boers, N., Rheinwalt, A., Bookhagen, B., Barbosa, H. M., Marwan, N., Marengo, J., & Kurths, J. (2014). The South American rainfall dipole: A complex network analysis of extreme events. *Geophysical Research Letters*, *41*(20), 7397–7405. https://doi.org/10.1002/2014GL061829

Bookhagen, B., & Strecker, M. R. (2008). Orographic barriers, high-resolution TRMM rainfall, and relief variations along the eastern Andes. *Geophysical Research Letters*, *35*(6), L06403. https://doi.org/10.1029/2007GL032011

Bowerman, A., Fu, R., Yin, L., Fernando, D. N., Arias, P. A., & Dickinson, R. E. (2017). An influence of extreme southern hemisphere cold surges on the North Atlantic Subtropical High through a shallow atmospheric circulation. *Journal of Geophysical Research: Atmospheres*, *122*(10), 135–148. https://doi.org/10.1002/2017JD026697

Carvalho, L. M. V., Jones, C., & Liebmann, B. (2002). Extreme precipitation events in southeastern South America and large-scale convective patterns in the South Atlantic convergence zone. *Journal of Climate*, *15*(17), 2377–2394. https://doi.org/10.1175/1520-0442(2002)015<2377:EPEISS>2.0.CO;2

Charney, J. G. (1969). A further note on large-scale motions in the tropics. *Journal of the Atmospheric Sciences*, *26*(1), 182–185. https://doi.org/10.1175/1520-0469(1969)026<0182:AFNOLS>2.0.CO;2

Chen, J., Hu, X., Yang, S., Lin, S., & Li, Z. (2022). Influence of convective heating over the maritime continent on the West Antarctic climate. *Geophysical Research Letters*, *49*(9), e2021GL097322. https://doi.org/10.1029/2021GL097322

Chen, M., Shi, W., Xie, P., Silva, V. B. S., Kousky, V. E., Higgins, R. W., & Janowiak, J. E. (2008). Assessing objective techniques for gauge-based analyses of global daily precipitation. *Journal of Geophysical Research*, *113*(D4), D04110. https://doi.org/10.1029/2007JD009132

Chen, S., & Wu, R. (2018). Impacts of early autumn Arctic sea ice concentration on subsequent spring Eurasian surface air temperature variations. *Climate Dynamics*, *51*(7), 2523–2542. https://doi.org/10.1007/s00382-017-4026-x

Chen, W., Hans-F, G., & Masaaki, T. (2002). Observed interannual oscillations of planetary wave forcing in the Northern Hemisphere winter. *Geophysical Research Letters*, *29*, 2073. https://doi.org/10.1029/2002GL016062

Cherchi, A., Carril, A. F., Menéndez, C. G., & Zamboni, L. (2014). La Plata Basin precipitation variability in spring: Role of remote SST forcing as simulated by GCM experiments. *Climate Dynamics*, *42*(1–2), 219–236. https://doi.org/10.1007/s00382-013-1768-y

Copernicus Climate Change Service. (2017). ERA5: Fifth generation of ECMWF atmospheric reanalyses of the global climate [Dataset]. Copernicus Climate Change Service Climate Data Store (CDS). Retrieved from https://cds.climate.copernicus.eu/cdsapp#!/home

Danard, M. B. (1964). On the influence of released latent heat on cyclone development. *Journal of Applied Meteorology*, *3*(1), 27–37. https://doi.org/10.1175/1520-0450(1964)003<0027:OTIORL>2.0.CO;2

Díaz, N., Barreiro, M., & Rubido, N. (2020). Intraseasonal predictions for the South American rainfall dipole. *Geophysical Research Letters*, *47*(21), e2020GL089985. https://doi.org/10.1029/2020GL089985

Dickinson, R. E. (1968). Planetary rossby waves propagating vertically through weak westerly wind wave guides. *Journal of the Atmospheric Sciences*, *25*(6), 984–1002. https://doi.org/10.1175/1520-0469(1968)025<0984:PRWPVT>2.0.CO;2

Dominguez, F., Eiras-Barca, J., Yang, Z., Bock, D., Nieto, R., & Gimeno, L. (2022). Amazonian moisture recycling revisited using WRF with water vapor tracers. *Journal of Geophysical Research: Atmospheres*, *127*(4), e2021JD035259. https://doi.org/10.1029/2021JD035259

Durkee, J. D., Mote, T. L., & Shepherd, J. M. (2009). The contribution of mesoscale convective complexes to rainfall across subtropical South America. *Journal of Climate*, *22*(17), 4590–4605. https://doi.org/10.1175/2009JCLI2858.1

Dwyer, J. G., & O'Gorman, P. A. (2017). Moist formulations of the Eliassen–Palm flux and their connection to the surface westerlies. *Journal of the Atmospheric Sciences*, *74*(2), 513–530. https://doi.org/10.1175/JAS-D-16-0111.1

Edmon, H. J., Hoskins, B. J., & McIntyre, M. E. (1980). Eliassen-Palm cross sections for the troposphere. *Journal of the Atmospheric Sciences*, *37*(12), 2600–2616. https://doi.org/10.1175/1520-0469(1980)037<2600:EPCSFT>2.0.CO;2

Efron, B., & Tibshirani, R. J. (1994). *An introduction to the bootstrap* (pp. 220–223). Chapman & Hall/CRC Press. Retrieved from https://www.routledge.com/An-Introduction-to-the-Bootstrap/Efron-Tibshirani/p/book/9780412042317

Emanuel, K. A., Fantini, M., & Thorpe, A. J. (1987). Baroclinic instability in an environment of small stability to slantwise moist convection. Part I: Two-dimensional models. *Journal of the Atmospheric Sciences*, *44*(12), 1559–1573. https://doi.org/10.1175/1520-0469(1987)044<1559:BIIAEO>2.0.CO;2

Feldstein, S. B. (2003). The dynamics of NAO teleconnection pattern growth and decay. *Quarterly Journal of the Royal Meteorological Society*, *129*(589), 901–924. https://doi.org/10.1256/qj.02.76

Gedney, N., & Valdes, P. J. (2000). The effect of Amazonian deforestation on the Northern Hemisphere circulation and climate. *Geophysical Research Letters*, *27*(19), 3053–3056. https://doi.org/10.1029/2000GL011794

Gelbrecht, M., Boers, N., & Kurths, J. (2018). Phase coherence between precipitation in South America and Rossby waves. *Science Advances*, *4*(12), eaau3191. https://doi.org/10.1126/sciadv.aau3191

Ghil, M., & Mo, K. C. (1991). Intraseasonal oscillations in the global atmosphere. Part II: Southern Hemisphere. *Journal of the Atmospheric Sciences*, *48*(5), 780–790. https://doi.org/10.1175/1520-0469(1991)048<0780:IOITGA>2.0.CO;2

Golding, B. (1984). A study of the structure of mid-latitude depressions in a numerical model using trajectory techniques. I: Development of ideal baroclinic waves in dry and moist atmospheres. *Quarterly Journal of the Royal Meteorological Society*, *110*(466), 847–879. https://doi.org/10.1002/qj.49711046605

Gong, T., Feldstein, S. B., & Lee, S. (2020). Rossby wave propagation from the Arctic into the midlatitudes: Does it arise from in situ latent heating or a trans-Arctic wave train? *Journal of Climate*, *33*(9), 3619–3633. https://doi.org/10.1175/JCLI-D-18-0780.1

Grimm, A. M., Barros, V. R., & Doyle, M. E. (2000). Climate variability in southern South America associated with El Niño and La Niña events. *Journal of Climate*, *13*(1), 35–58. https://doi.org/10.1175/1520-0442(2000)013<0035:CVISSA>2.0.CO;2

Gulev, S. K., Jung, T., & Ruprecht, E. (2002). Climatology and interannual variability in the intensity of synoptic-scale processes in the North Atlantic from the NCEP–NCAR reanalysis data. *Journal of Climate*, *15*(8), 809–828. https://doi.org/10.1175/1520-0442(2002)015<0809:CAIVIT>2.0.CO;2

Gutowski, W. J., Jr., Branscome, L. E., & Stewart, D. A. (1992). Life cycles of moist baroclinic eddies. *Journal of the Atmospheric Sciences*, *49*(4), 306–319. https://doi.org/10.1175/1520-0469(1992)049<0306:LCOMBE>2.0.CO;2

Gyakum, J. R. (1983). On the evolution of the QE II storm. II: Dynamic and thermodynamic structure. *Monthly Weather Review*, *111*(6), 1156–1173. https://doi.org/10.1175/1520-0493(1983)111<1156:OTEOTI>2.0.CO;2

Held, I. M., Panetta, R. L., & Pierrehumbert, R. T. (1985). Stationary external Rossby waves in vertical shear. *Journal of the Atmospheric Sciences*, *42*(9), 865–883. https://doi.org/10.1175/1520-0469(1985)042<0865:SERWIV>2.0.CO;2

Hoskins, B. J., & Yang, G.-Y. (2000). The equatorial response to higher-latitude forcing. *Journal of the Atmospheric Sciences*, *57*(9), 1197–1213. https://doi.org/10.1175/1520-0469(2000)057<1197:TERTHL>2.0.CO;2

Hsu, H. H., & Lin, S. H. (1992). Global teleconnections in the 250-mb streamfunction field during the in the geopotential height field during the Northern Hemisphere winter. *Monthly Weather Review*, *120*(7), 1169–1190. https://doi.org/10.1175/1520-0493(1992)120<1169:GTITMS>2.0.CO;2

Hu, D., Guan, Z., Tian, W., & Ren, R. (2018). Recent strengthening of the stratospheric Arctic vortex response to warming in the central North Pacific. *Nature Communications*, *9*(1), 1–10. https://doi.org/10.1038/s41467-018-04138-3

Jones, C., & Carvalho, L. M. (2002). Active and break phases in the South American monsoon system. *Journal of Climate*, *15*(8), 905–914. https://doi.org/10.1175/1520-0442(2002)015<0905:AABPIT>2.0.CO;2

Karoly, D. J. (1983). Rossby wave propagation in a barotropic atmosphere. *Dynamics of Atmospheres and Oceans*, *7*(2), 111–125. https://doi.org/10.1016/0377-0265(83)90013-1

Lapeyre, G., & Held, I. (2004). The role of moisture in the dynamics and energetics of turbulent baroclinic eddies. *Journal of the Atmospheric Sciences*, *61*(14), 1693–1710. https://doi.org/10.1175/1520-0469(2004)061<1693:TROMIT>2.0.CO;2

Lau, K. M., & Li, M. T. (1984). The monsoon of East Asia and its global associations—A survey. *Bulletin of the American Meteorological Society*, *65*(2), 114–125. https://doi.org/10.1175/1520-0477(1984)065<0114:TMOEAA>2.0.CO;2

Lenters, J. D., & Cook, K. H. (1997). On the origin of the Bolivian high and related circulation features of the South American climate. *Journal of the Atmospheric Sciences*, *54*(5), 656–678. https://doi.org/10.1175/1520-0469(1997)054<0656:OTOOTB>2.0.CO;2

Li, T. (2006). Origin of the summertime synoptic-scale wave train in the Western north Pacific. *Journal of the Atmospheric Sciences*, *63*(3), 1093–1102. https://doi.org/10.1175/JAS3676.1

Li, W., & Fu, R. (2004). Transition of the large-scale atmospheric and land surface conditions from the dry to the wet season over Amazonia as diagnosed by the ECMWF re-Analysis. *Journal of Climate*, *17*(13), 2637–2651. https://doi.org/10.1175/1520-0442(2004)017<2637:TOTLAA>2.0.CO;2

Li, Y., Feng, J., Li, J., & Hu, A. (2019). Equatorial windows and barriers for stationary Rossby wave propagation. *Journal of Climate*, *32*(18), 6117–6135. https://doi.org/10.1175/JCLI-D-18-0722.1

Li, Y., Li, J., Jin, F. F., & Zhao, S. (2015). Interhemispheric propagation of stationary Rossby waves in a horizontally nonuniform background flow. *Journal of the Atmospheric Sciences*, *72*(8), 3233–3256. https://doi.org/10.1175/JAS-D-14-0239.1

Lieberman, R. S. (1999). Eliassen-Palm fluxes of the 2-day wave. *Journal of the Atmospheric Sciences*, *56*(16), 2846–2861. https://doi.org/10.1175/1520-0469(1999)056<2846:EPFOTD>2.0.CO;2

Liebmann, B., Kiladis, G. N., Carvalho, L. M. V., Jones, C., Vera, C. S., Bladé, L., & Allured, D. (2009). Origin of convectively coupled Kelvin waves over South America. *Journal of Climate*, *22*(2), 300–315. https://doi.org/10.1175/2008JCLI2340.1

Liebmann, B., Kiladis, G. N., Vera, C. S., Saulo, A. C., & Carvalho, L. M. (2004). Subseasonal variations of rainfall in South America in the vicinity of the low-level jet east of the Andes and comparison to those in the South Atlantic convergence zone. *Journal of Climate*, *17*(19), 3829–3842. https://doi.org/10.1175/1520-0442(2004)017<3829:SVORIS>2.0.CO;2

Liebmann, B., & Mechoso, C. R. (2011). The South American monsoon system. In C.-P. Chang, Y. Ding, N.-C. Lau, R. H Johnson, B. Wang, & T. Yasunari (Eds.), *The global monsoon system: Research and forecast* (2nd ed., pp. 137–157). World Scientific. https://doi.org/10.1142/9789814343411_0009

Luo, D., Diao, Y., & Feldstein, S. B. (2011). The variability of the Atlantic storm track and the North Atlantic oscillation: A link between intraseasonal and interannual variability. *Journal of the Atmospheric Sciences*, *68*(3), 577–601. https://doi.org/10.1175/2010JAS3579.1

Lutsko, N. J. (2018). The response of an idealized atmosphere to localized tropical heating: Superrotation and the breakdown of linear theory. *Journal of the Atmospheric Sciences*, *75*(1), 3–20. https://doi.org/10.1175/JAS-D-17-0192.1

Marengo, J. A., Liebmann, B., Grimm, A. M., Misra, V., Silva Dias, P. L., Cavalcanti, I. F. A., et al. (2012). Recent developments on the South American monsoon system. *International Journal of Climatology*, *32*(1), 1–21. https://doi.org/10.1002/joc.2254

Marengo, J. A., Soares, W. R., Saulo, C., & Nicolini, M. (2004). Climatology of the low-level jet east of the Andes as derived from the NCEP-NCAR reanalyses: Characteristics and temporal variability. *Journal of Climate*, *17*(12), 2261–2280. https://doi.org/10.1175/1520-0442(2004)017<2261:COTLJE>2.0.CO;2

Marengo, J. A., Valverde, M. C., & Obregon, G. O. (2013). Observed and projected changes in rainfall extremes in the metropolitan area of Sao Paulo. *Climate Research*, *57*(1), 61–72. https://doi.org/10.3354/cr01160

Mayta, V. C., Kiladis, G. N., Dias, J., Silva Dias, P. L., & Gehne, M. (2021). Convectively coupled Kelvin waves over tropical South America. *Journal of Climate*, *34*, 6531–6547. https://doi.org/10.1175/JCLI-D-20-0662.1

Mo, K. C., & Ghil, M. (1987). Statistics and dynamics of persistent anomalies. *Journal of the Atmospheric Sciences*, *44*(5), 877–902. https://doi.org/10.1175/1520-0469(1987)044<0877:SADOPA>2.0.CO;2

Mo, K. C., & Paegle, J. N. (2001). The Pacific-South American modes and their downstream effects. *International Journal of Climatology*, *21*(10), 1211–1229. https://doi.org/10.1002/joc.685

Montini, T. L., Jones, C., & Carvalho, L. M. V. (2019). The South American low-level jet: A new climatology, variability, and changes. *Journal of Geophysical Research: Atmospheres*, *124*(3), 1200–1218. https://doi.org/10.1029/2018JD029634

NOAA CPC. (2008). CPC global unified gauge-based analysis of daily precipitation [Dataset]. NOAA CPC. Retrieved from https://psl.noaa.gov/data/gridded/data.cpc.globalprecip.html

Nogués-Paegle, J., & Mo, K. C. (1997). Alternating wet and dry conditions over South America during summer. *Monthly Weather Review*, *125*(2), 279–291. https://doi.org/10.1175/1520-0493(1997)125<0279:AWADCO>2.0.CO;2

Paegle, J. N., Byerle, L. A., & Mo, K. C. (2000). Intraseasonal modulation of South American summer precipitation. *Monthly Weather Review*, *128*(3), 837–850. https://doi.org/10.1175/1520-0493(2000)128<0837:IMOSAS>2.0.CO;2

Salio, P., Nicolini, M., & Zipser, E. J. (2007). Mesoscale convective systems over Southeastern South America and their relationship with the South American low-level jet. *Monthly Weather Review*, *135*(4), 1290–1309. https://doi.org/10.1175/MWR3305.1

Silva Dias, P. L., Schubert, W. H., & DeMaria, M. (1983). Large-scale response of the tropical atmosphere to transient convection. *Journal of the Atmospheric Sciences*, *40*(11), 2689–2707. https://doi.org/10.1175/1520-0469(1983)040<2689:LSROTT>2.0.CO;2

Silvestri, G. E., & Vera, C. S. (2003). Antarctic oscillation signal on precipitation anomalies over southeastern South America. *Geophysical Research Letters*, *30*(21), 2115. https://doi.org/10.1029/2003GL018277

Snyder, P. K. (2010). The influence of tropical deforestation on the northern hemisphere climate by atmospheric teleconnections. *Earth Interactions*, *14*(4), 1–34. https://doi.org/10.1175/2010EI280.1

Ting, M. (1996). Steady linear response to tropical heating in barotropic and baroclinic models. *Journal of the Atmospheric Sciences*, *53*(12), 1698–1709. https://doi.org/10.1175/1520-0469(1996)053<1698:SLRTTH>2.0.CO;2

Tomas, R. A., & Webster, P. J. (1994). Horizontal and vertical structure of cross-equatorial wave propagation. *Journal of the Atmospheric Sciences*, *51*(11), 1417–1430. https://doi.org/10.1175/1520-0469(1994)051<1417:HAVSOC>2.0.CO;2

Vera, C., Higgins, W., Amador, J., Ambrizzi, T., Garreaud, R., Gochis, D., et al. (2006). Toward a unified view of the American monsoon systems. *Journal of Climate*, *19*(20), 4977–5000. https://doi.org/10.1175/JCLI3896.1

Vera, C. S., Alvarez, M. S., Gonzalez, P. L. M., Liebmann, B., & Kiladis, G. N. (2018). Seasonal cycle of precipitation variability in South America on intraseasonal timescales. *Climate Dynamics*, *51*(5–6), 1991–2001. https://doi.org/10.1007/s00382-017-3994-1

Wallace, J. M., & Gutzler, D. S. (1981). Teleconnections in the geopotential height field during the northern hemisphere winter. *Monthly Weather Review*, *109*(4), 784–812. https://doi.org/10.1175/1520-0493(1981)109<0784:TITGHF>2.0.CO;2

Wang, H., & Fu, R. (2002). Cross-equatorial flow and seasonal cycle of precipitation over South America. *Journal of Climate*, *15*(13), 1591–1608. https://doi.org/10.1175/1520-0442(2002)015<1591:CEFASC>2.0.CO;2

Webster, P. J., & Holton, J. R. (1982). Cross-equatorial response to middle-latitude forcing in a zonally varying basic state. *Journal of the Atmospheric Sciences*, *39*(4), 722–733. https://doi.org/10.1175/1520-0469(1982)039<0722:CERTML>2.0.CO;2

Werth, D., & Avissar, R. (2002). The local and global effects of Amazon deforestation. *Journal of Geophysical Research*, *107*(D20), 8087. https://doi.org/10.1029/2001JD000717

Wirth, V., Riemer, M., Chang, E. K. M., & Martius, O. (2018). Rossby wave packets on the midlatitude waveguide—A review. *Monthly Weather Review*, *146*(7), 1965–2001. https://doi.org/10.1175/MWR-D-16-0483.1

Wright, J., Fu, R., Fu, R., John, W. R., Chakraborty, S., Clinton, N. E., et al. (2017). Rainforest-initiated wet season onset over the southern Amazon. *Proceedings of the National Academy of Sciences of the United States of America*, *114*(32), 8481–8486. https://doi.org/10.1073/pnas.1621516114

Yang, S., & Webster, P. J. (1990). The effect of summer tropical heating on the location and intensity of the extratropical westerly jet streams. *Journal of Geophysical Research*, *95*(11), 705–718. https://doi.org/10.1029/JD095iD11p18705

Zamboni, L., Mechoso, C., & Kucharski, F. (2010). Relationships between upper-level circulation over South America and rainfall over southeastern South America: A physical base for seasonal predictions. *Journal of Climate*, *23*(12), 3300–3315. https://doi.org/10.1175/2009JCLI3129.1

Zhang, C., Nolan, D. S., Thorncroft, C. D., & Nguyen, H. (2008). Shallow meridional circulations in the tropical atmosphere. *Journal of Climate*, *21*(14), 3453–3470. https://doi.org/10.1175/2007JCLI1870.1

Zhang, J., Guan, K., Fu, R., Peng, B., Zhao, S., & Zhuang, Y. (2023). Evaluating seasonal climate forecasts from dynamical models over South America. *Journal of Hydrometeorology*, *24*(4), 801–814. https://doi.org/10.1175/JHM-D-22-0156.1

Zhao, S., Deng, Y., & Black, R. X. (2018). An intraseasonal mode of atmospheric variability relevant to the US hydroclimate in boreal summer: Dynamic origin and East Asia connection. *Journal of Climate*, *31*(24), 9855–9868. https://doi.org/10.1175/JCLI-D-18-0206.1

Zhao, S., & Fu, R. (2022). The influence of convectively coupled Kelvin waves on Atlantic Niños. *Journal of Geophysical Research: Atmospheres*, *127*(9), e2021JD036241. https://doi.org/10.1029/2021JD036241

Zhao, S., Li, J., Li, Y., Jin, F.-F., & Zheng, J. (2019). Interhemispheric influence of Indo-Pacific convection oscillation on Southern Hemisphere rainfall through southward propagation of Rossby waves. *Climate Dynamics*, *52*(5–6), 3203–3221. https://doi.org/10.1007/s00382-018-4324-y

Zhao, S., Li, J. P., & Li, Y. J. (2015). Dynamics of an interhemispheric teleconnection across the critical latitude through a southerly duct during boreal winter. *Journal of Climate*, *28*(19), 7437–7456. https://doi.org/10.1175/JCLI-D-14-00425.1

Zhong, W., Cai, W., Sullivan, A., Duan, W., & Yang, S. (2023). Seasonally alternate roles of the North Pacific oscillation and the South Pacific oscillation in tropical Pacific zonal wind and ENSO. *Journal of Climate*, *36*(13), 4393–4411. https://doi.org/10.1175/JCLI-D-22-0461.1

Zhou, J., & Lau, K.-M. (1998). Does a monsoon climate exist over South America? *Journal of Climate*, *11*(5), 1020–1040. https://doi.org/10.1175/1520-0442(1998)011<1020:DAMCEO>2.0.CO;2

Zhu, Z., & Li, T. (2016). A new paradigm for continental U.S. summer rainfall variability: Asia–North America teleconnection. *Journal of Climate*, *29*(20), 7313–7327. https://doi.org/10.1175/JCLI-D-16-0137.1